International Journal of Solids and Structures 48 (2011) 175–190

Contents lists available at ScienceDirect

International Journal of Solids and Structures

journal homepage: www.elsevier.com/locate/ijsolstr

# Analysis of Knoop indentation

A.E. Giannakopoulos, Th. Zisis *

*Laboratory of Strength of Materials and Micromechanics, Department of Civil Engineering, University of Thessaly, Volos 38336, Greece*

ARTICLE INFO

*Article history:*
Received 15 June 2010
Received in revised form 27 August 2010
Available online 25 September 2010

*Keywords:*
Mechanics of indentation
Knoop
Finite element method
Elastoplasticity

ABSTRACT

Knoop indentation tests have long been a standard method for material characterization due to the fact that they provide an easy, inexpensive non destructive and objective method of evaluating basic properties from small volumes of materials. In spite of the broad use, Knoop indentation has never been analysed and its methodology is basically empirical. The present work presents an extensive finite element study on the adhesionless contact of flat surfaces by Knoop indenter. The aim of this work is to explore the theoretical foundation for the commonly used Knoop test and shed light to the interesting details that make the Knoop test so useful and simple. Both elastic and elastoplastic responses are explored. The material of the contacting solid is modeled as homogeneous and isotropic. The effect of the Coulomb friction at the contact region is also considered. Subsequently, the computational results presented in the current study are compared with analytical and experimental results that exist in bibliography.



## 1. Introduction

Indentation tests have long been a standard method for material characterization, Tabor (1951) and Mott (1956). When testing materials in layered components of micro-electro-mechanical devices, polymer films, paintings, biomaterials, etc. the volumes under investigation are very small while the environmental conditions can make classical mechanical tests difficult to perform. Such conditions may arise when materials operate at cryogenic temperatures, in devices like superconducting electric circuits, liquid hydrogen bubble chambers and cryogenic fuelled rockets or at low temperatures that reduce phenomena such as thermal vibration and diffusion and allow fundamental studies on dislocation movements. In such conditions micro-indentations are good alternative tests that can be adopted to perform in harsh environments, however they require accurate analysis.

In recent years, instrumented indentation, using preferably pyramid indenters such as Vickers, Berckovich and Knoop, proved to be very useful in testing small material volumes, Fischer-Cripps (2002). Although instrumented indentation has been in use for more than 20 years, fundamental issues remain to be cleared. Such issues include the systematic investigation of the elastic and elasto-plastic indentation by pyramid indenters. Standard geometries for pyramid indenters are three types of pyramids under the well established terms of Smith and Sutherland (1925), Berkovich (1951) and Knoop et al. (1939). Their shapes are normal pyramids with square, regular triangle and rhombus bases, respectively. Their tips are unavoidably slightly rounded; however, the influence of roundness is not always of major concern, especially when indentation is sufficiently deep. The main obstacle for such investigations is the difficulty in the non-linearity of the contact analysis and the computational demands that present the three-dimensional aspects of the problem.

Numerical work on the subject has been attempted in recent years. The Vickers and Berkovich indentation methods have been examined by Giannakopoulos et al. (1994), Murakami et al. (1994) and Larsson et al. (1996), respectively. In these works the finite element method (FEM) was incorporated in three-dimensional models in order to explore the theoretical foundation for the commonly used tests while the response for isotropic elasticity and large elastoplastic deformations was examined. The theoretical findings were compared with experimental results, performed both on the nano- and microscale.

On the other hand, the Knoop indentation has not received the appropriate attention in terms of theoretical investigation. Because Knoop indentation is less symmetric than Vickers and Berkovich indentation, its numerical analysis is harder to perform. The only numerical work on Knoop indentation that we are aware of was presented by Rabinovich and Savin (1996) where a new methodology for solution of the three-dimensional contact based on the variational and boundary integral approach was developed, in the context of linear elasticity. Rabinovich and Savin presented approximately the shape of the contact pressure field as well as the shape of the contact area. Furthermore, Giannakopoulos (2006) presented analytical results of frictionless and adhesionless contact of flat, linear elastic and viscoelastic isotropic surfaces by pyramid indenters. His analysis considered the standard shapes

* Corresponding author. Tel.: +30 24210 74179; fax: +30 24210 74169.
*E-mail address:* zisis@metal.ntua.gr (Th. Zisis).

0020-7683/$ - see front matter © 2010 Elsevier Ltd. All rights reserved.
doi:10.1016/j.ijsolstr.2010.09.014

of Vickers, Berkovich and Knoop pyramids and the results included explicit relations between the normal applied load and depth of penetration, details of the contact area shapes, the surface stresses and the contact pressure distribution. The results were complemented by experimental investigations and for the case of Vickers and Berkovich indenters, numerical results existing in bibliography were added.

Due to the limited theoretical analysis of the Knoop indentation, an extensive numerical analysis of the problem is in need. The reduced symmetry of the problem calls for full three-dimensional finite element analysis. The computational burden increases dramatically, if the non-linear deformation, elasto-plastic material response and frictional contact conditions are taken into account. This work will take all previous aspects into account and will clarify the special characteristics of the problem, such as the force versus displacement curves, the attained displacement and stress fields, the contact area, etc.

In what follows, we present the method and the acquired results that clarify the scope of this investigation. Due the nonlinearities involved, we rely heavily upon the finite element method (FEM), while a considerable theoretical and numerical experience was drawn from work done by Storakers and Larsson (1993), Wang and Bangert (1993), Olaf (1993), Zeng and Rowcliffe (1994), Giannakopoulos et al. (1994) and Giannakopoulos (2006).

## 2. Problem formulation

The geometrical characteristics of the Knoop indentation test are shown schematically in Fig. 1. The three characteristic surfaces folding the area of interest are shown. We define as $h$ the indentation depth, as $l$ the contact radius along the $x$-direction and as $m$ the contact radius along the $y$-direction. $\Theta$ and $\Phi$ are the included angles of the Knoop indenter as shown in the same figure. The true projection of the contact area is generally different from the shape of the pyramid base and we define another characteristic parameter of the problem, $\Phi_1$ as shown in Fig. 1. We assume a rigid indenter penetrating a homogeneous, isotropic, rate independent semi-infinite body. The geometric characteristics of the Knoop pyramid are described by the normal rhomboidal base with ratio of diameter 1:7.11, included longitudinal angle 172.5° and included transverse angle 130°. Knoop pyramid has only a twofold-symmetry, thus one forth of the problem needs to be modeled. In the case of Vickers indentation test, for example, only one eighth of the problem has to be modeled due to the eightfold symmetry of the specific indenter, extending at the deformation field, Giannakopoulos et al. (1994). One of the basic difficulties of the specific problem is the computational cost. In the case of material anisotropy or configurational instability, the whole body needs to be modeled. In this work, we will assume isotropy and configurational stability of the contact surface. Quasi-static, isothermal analysis was carried-out, and the indentation is assumed to take place so that dynamic effects, mainly due to the kinetic energy of the indenter, can be ignored. Bulk constitutive behavior was assumed for the indented body, which means that our results are meaningful for indentation depth $h$ that is much higher than the characteristic microstructural size of the indented material (grain size) and the tip roundness.

The indentation of the half space is a nonlinear problem. One main reason is that the contact area is not known *a priori*. A penalty approach method is used here for the contact pressure definition where the contact pressure at a point on the deformed surface $p_c$ is given as a function of the interpenetration $h_c$ of the contacting surfaces as predicted in the absence of the contact constraint

$$\begin{aligned} p_c &= 0; \quad h_c < 0, \\ p_c &= \bar{k} h_c; \quad h_c \geqslant 0. \end{aligned} \tag{1}$$

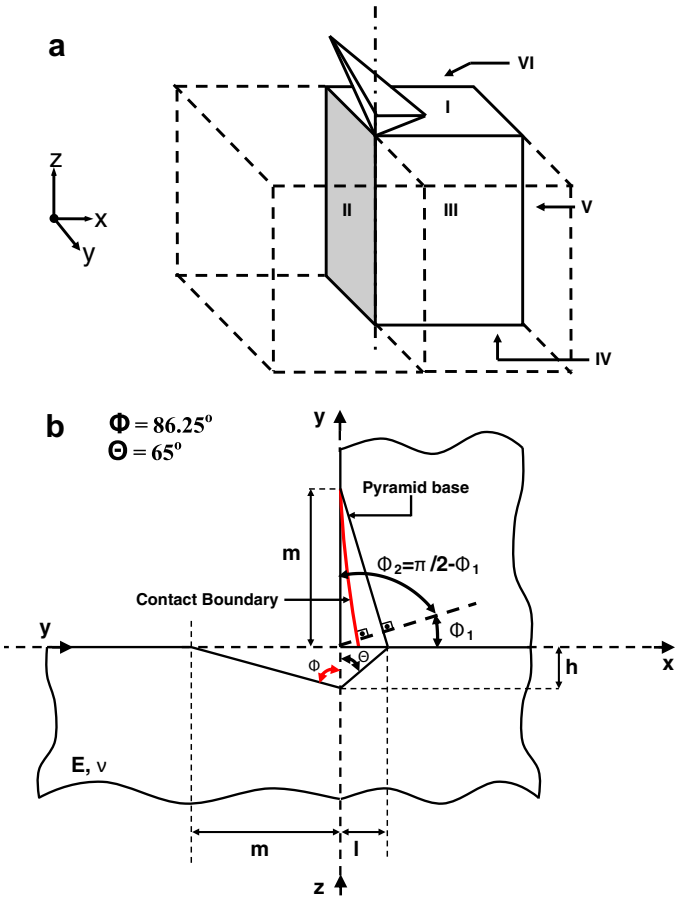


**Fig. 1.** (a) Schematic representation of the problem. The Knoop pyramid and the indented body. One-fourth of the domain is descretised due to symmetry. (b) The three surfaces of interest unfolded. Characteristic parameters of the problem are defined for pyramids with twofold-symmetry.

Here $\bar{k}$ is a large penalty coefficient resembling a very stiff spring constant. The limiting case of Eq. (1), as $\bar{k} \to \infty$ corresponds to the Signorini type of contact boundary condition (zero contact traction at the contact area perimeter). Previous indentation results showed a minor influence of friction on the contact analysis of spherical indenters (e.g. Bower et al., 1993; Li et al., 1993), as well as of Vickers indenters (Giannakopoulos et al., 1994). In the present work we investigate the influence of the Coulomb friction between the indenter and the substrate.

Computational difficulties of the problem rise due to the characteristic dimensions of the indenter and the resulting contact area is difficult to be handled computationally – that is very large ratio of $m/l$. Thus of great importance is the construction of a mesh that will provide high accuracy and at the same time efficiency of the FEM computations. A three-dimensional finite element mesh was constructed. Fig. 1a shows that the indented body is bounded by six characteristic surfaces. The nodes of planes II–IV can deform only in their own planes. Plane I is the indented surface which includes the contact elements. Plane IV (at a depth $r_v$ form the indented surface) has zero vertical displacements. The surfaces V and VI are traction free. The very fine mesh division close to the indenter's tip allows a good resolution of the contact area (see Fig. 2). The figures that contain the isocontours of various mechanical variables will be presented for the planes I–III. The FEM meshes were constructed in such a way in order to engulf the solution near the contact region by the elastic Boussinesq solution. Extensive numerical simulations of the problem, with different meshes, were undertaken in order to define the appropriate distance of the

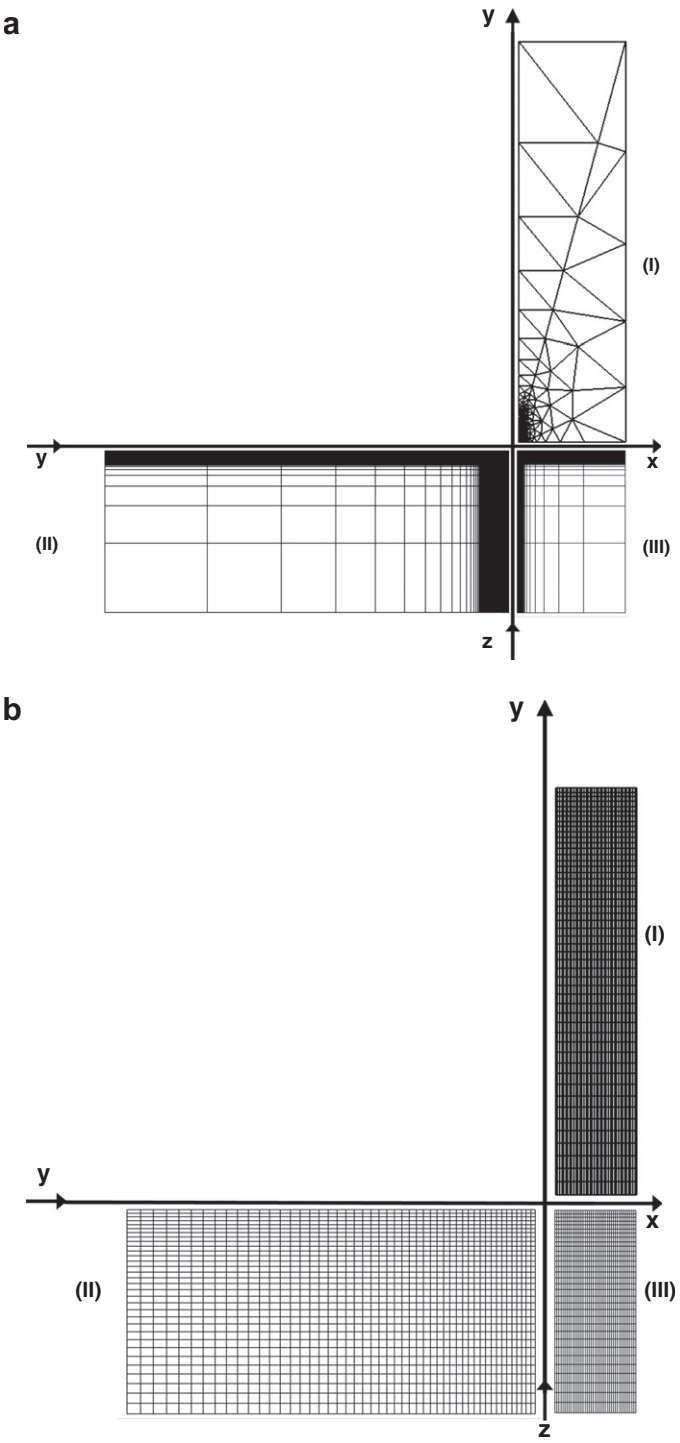


**Fig. 2.** (a) Typical mesh used for the simulations. (b) Blown-up view of the mesh around the region of interest (contact region and surrounding substrate).

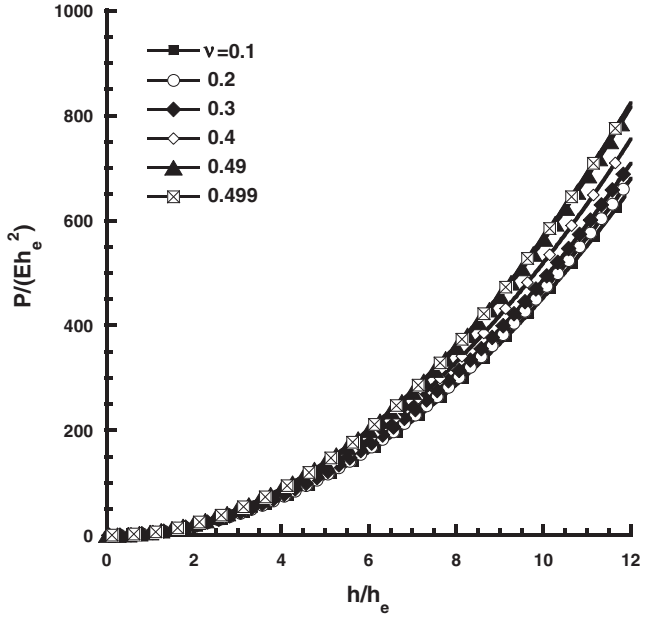


**Fig. 3.** Dimensionless load $P/\left(Eh_e^2\right)$ versus dimensionless indentation depth $h/h_e$ for different values of Poisson ratio. ($h_e$ is the minimum element length at the region of interest near the tip of the indenter).

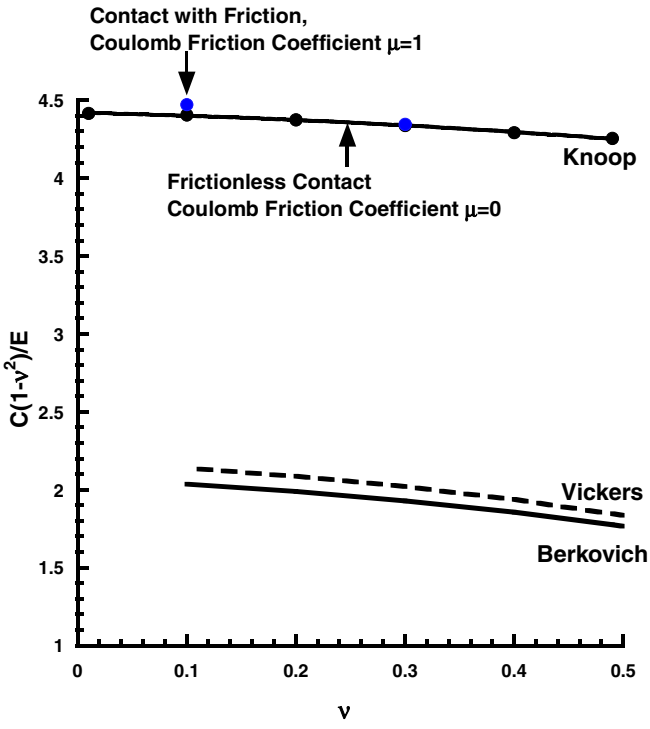


**Fig. 4.** Contact stiffness factor $C(1-\nu^2)/E = P(1-\nu^2)/(Eh^2)$ as a function of the Poisson ratio $\nu$. Corresponding results are given for Vickers and Berkovich pyramid indenters for comparison. For the case of Knoop, results are shown for frictionless contact conditions and for Coulomb friction coefficient $\mu = 1$.

boundaries in the three directions from the contact region. In the analysis, the boundary along the $x$-direction was taken to be 51 times the corresponding contact radius $l$, at the $y$-direction was taken to be 16 times the corresponding contact radius $m$ and at the $z$-direction was taken to be 84 times the indentation depth $h$. The minimum element length along the $x$-direction is designated as $h_e$. We conclude that the solution was mostly influenced by the outer boundary of the mesh along the $x$ and $z$-directions and appeared to be relative insensitive to the boundary along the $y$-axis. Furthermore, extensive testing of the mesh was undertaken to assess the element type, the node density, the element layout and the far field conditions which have to conform with Bussinesq solution of a point force normal to the surface of a semi-infinite elastic solid. Our mesh was also tested and compared with

solutions existing in the literature for the Vickers indentation (Giannakopoulos et al., 1994) and our numerical results, regarding the contact radius, the reaction force and the stress and displacement fields proved to be in agreement within 3%.

Based on the Vickers analysis of Giannakopoulos et al. (1994), the mesh shown in Fig. 2 was constructed for the Knoop indentation with the following characteristics: 73,883 nodes and a combination of 87,860 eight-noded isoparametric block elements and six noded isoparametric elements. The commercial finite element program ABAQUS Standard (2001) was employed for the numerical calculations. At the peak depth of indentation at least 11 elements spanned the contact radius in all directions. Large deformation effects were included by using the non-linear geometry option within ABAQUS Standard. Full numerical integration was used. The automatic stepping routine required about 1000 increments. The computations required about 200 h of CPU time on a computer with 3 Gb of RAM and a 2.67 GHz dual processor.

## 3. Elastic analysis

Hypoelastic analysis is assumed and in our formulation, the constitutive law integrated was

$$\hat{\tau}_{ij} = \frac{E}{1+\nu}\left[\delta_{ik}\delta_{jl} + \frac{\nu}{1-2\nu}\delta_{ij}\delta_{kl}\right] D_{kl}, \tag{2}$$

where $\hat{\tau}_{ij}$ is the co-rotational (Jaumman) rate of the Kirchhoff stress $\tau_{ij}$, $E$ is the Young's modulus and $\nu$ is the Poisson ratio. The Kirchhoff stress $\tau_{ij}$ is related to its total rate $\dot{\tau}_{ij}$ by the spin tensor $\Omega_{ij}$ as

$$\hat{\tau}_{ij} = \dot{\tau}_{ij} - (\Omega_{ik}\tau_{kj} + \tau_{il}\Omega_{lj}) \tag{3}$$

and

$$\Omega_{ij} = (\partial \dot{u}_i/\partial x_j - \partial \dot{u}_j/\partial x_i)/2, \tag{4}$$

where $\dot{u}_i$ is the material velocity and $x_i$ is the current position of a material point at $X_i$. The deformation mapping is $x_i = X_i + u_i$. Finally, $D_{ij}$ is the rate of deformation defined as

$$D_{ij} = (\partial \dot{u}_i/\partial x_j + \partial \dot{u}_j/\partial x_i)/2. \tag{5}$$

The Kirchhoff stresses $\tau_{ij}$ are related to the Cauchy stresses $\sigma_{ij}$ through $\tau_{ij} = J\sigma_{ij}$, where $J$ is the determinant of the deformation gradient tensor $(\partial x_i/\partial X_j)$. Note that $J > 0$ is the condition of impenetrability of matter. In the absence of body and inertia forces, the equilibrium equations that have to be satisfied in the entire body are

$$\partial \sigma_{ij}/\partial x_j = 0. \tag{6}$$

We note that a small strain formulation analysis was conducted, as well, using the same elastic constants but it gave similar bulk and field results with the hypoelastic formulation analysis. This appears to be in agreement with the results of Giannakopoulos et al. (1994). Accordingly the results that will be presented, in what follows, fall in the frame of hypoelasticity.

The applied vertical displacement of the indenter was related to the reaction load on the indenter (Fig. 3). The results are shown in non-dimensional form for different values of the Poisson ratio $\nu$, where $h_e$ is the minimum element length along the $x$-direction (the length of the first element in contact). The indentation depth is the only characteristic length of the problem and from dimensional considerations; the average pressure must be constant. This indicates a parabolic relation between total load $P$ and indentation depth $h$ of the general form $P = Ch^2$, where $C$ is a function of the

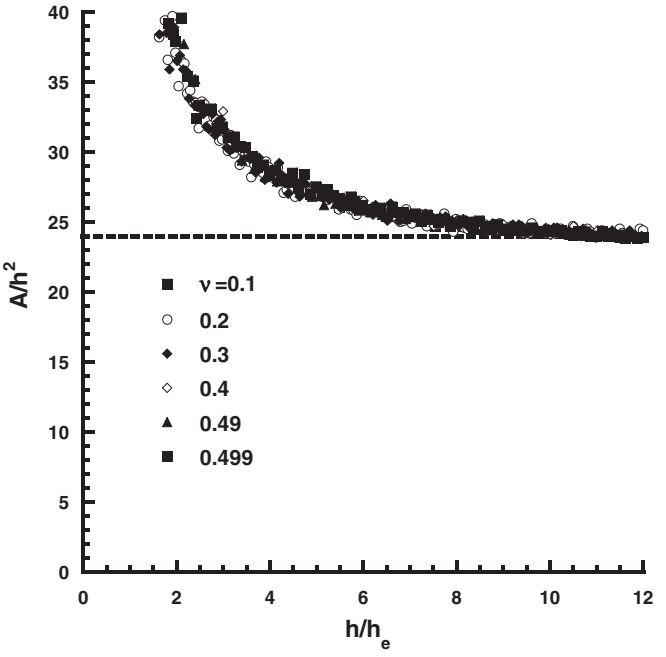


**Fig. 5.** The rate of numerical convergence. Dimensionless contact area $A/h^2$ as a function of the dimensionless indentation depth $h/h_e$. Results are shown for different values of Poisson ratio.

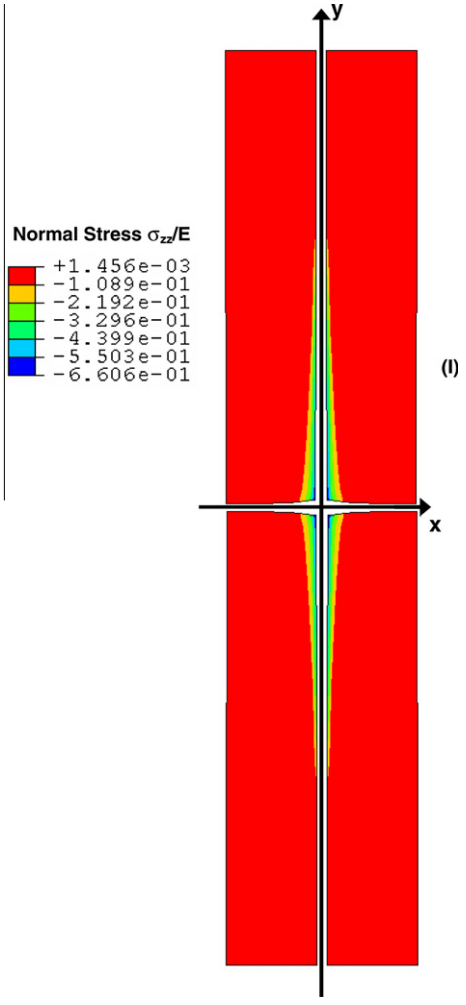


**Fig. 6.** Contours of dimensionless $\sigma_{zz}/E$ stresses for Poisson ratio $\nu = 0.3$. The characteristic geometry of the contact area is evident (the contact perimeter is the curve $\sigma_{zz}/E = 0$.

Poisson ratio. Numerically the parabolic relation was actually confirmed.

The coefficient $C$ calculated as $C = P/h^2$ is constant for $h/h_e \geqslant 10$. The independent parameter of the problem is the Poisson ratio $\nu$. The effect of the Poisson ratio on $C$ is observed in Fig. 4 and by fitting the numerical results, we conclude that $C$ is related to the elastic properties as:

$$C(1-\nu^2)/E = 4.4146(1 - 0.002178\nu + 0.2887\nu^2 - 0.2691\nu^3). \tag{7a}$$

Nevertheless the Poisson ratio seems to be of minor importance, because the displacements tangent to the contact surface are very small compared to the indentation depth. For comparison we write the corresponding solutions for Vickers and Berkovich indentations (see Giannakopoulos et al., 1994; Larsson et al., 1996 respectively):

$$C(1-\nu^2)/E = 2.0746(1 - 0.1655\nu - 0.1737\nu^2 - 0.1862\nu^3), \tag{7b}$$

$$C(1-\nu^2)/E = 2.1891(1 - 0.21\nu - 0.01\nu^2 - 0.41\nu^3). \tag{7c}$$

We confirm that the displacements, tangent to the contact surface, are much smaller for the Knoop case and that the indentation with the Knoop indenter gives a value of $C$ about two times higher than that provided by the Vickers and Berkovich indenters. This suggests better resolution characteristics of the Knoop $P$–$h$ curve in an indentation experiment when compared to the other two pyramid indenters. Note that the effect of Coulomb friction ($\mu = 1$) is of minor importance.

We now turn our attention to the contact area $A$ projected to the initial flat surface (i.e. contact area as seen from the normal to the surface $z$-direction). Again the contact area follows a parabolic relation with respect to the indentation depth according to $A = Kh^2$. In Fig. 5 we present the parameter $K = A/h^2$ as a function of the dimensionless indentation depth $h/h_e$ for different values of the Poisson ratio. It is concluded that $A/h^2$ drops, with increasing indentation depth, to a steady value of 23.95 which corresponds to indentation depths $h/h_e \geqslant 10$. At such levels we can be sure that the solution has converged. The variation of $A/h^2$ with depth $h$ (or load $P$) is only a feature of the computation evolution of $A$ and is due to the poor resolution of $A$ for $h/h_e \leqslant 10$. Fig. 5, presents

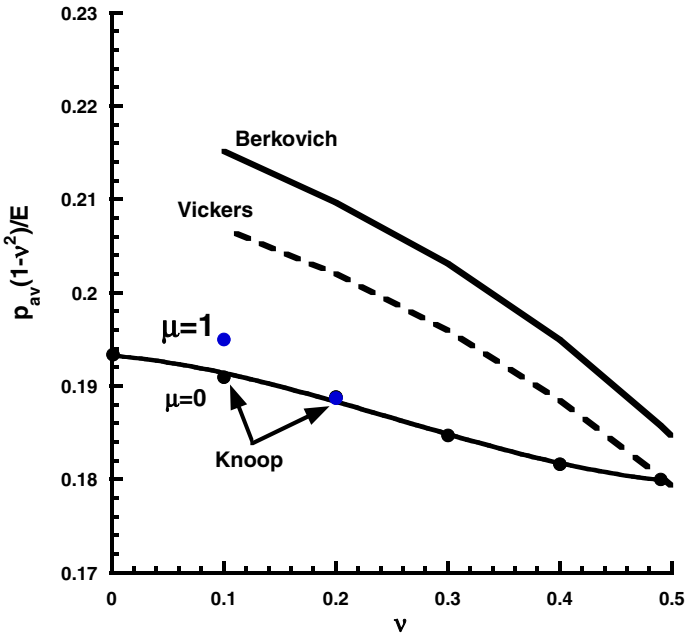


**Fig. 7.** Average pressure $p_{av}(1-\nu^2)/E$ as a function of the Poisson ratio $\nu$. Analytical results are given for Vickers and Berkovich pyramid indenters for comparison. For the case of Knoop, results are shown for frictionless contact conditions and for Coulomb friction coefficient $\mu = 1$.

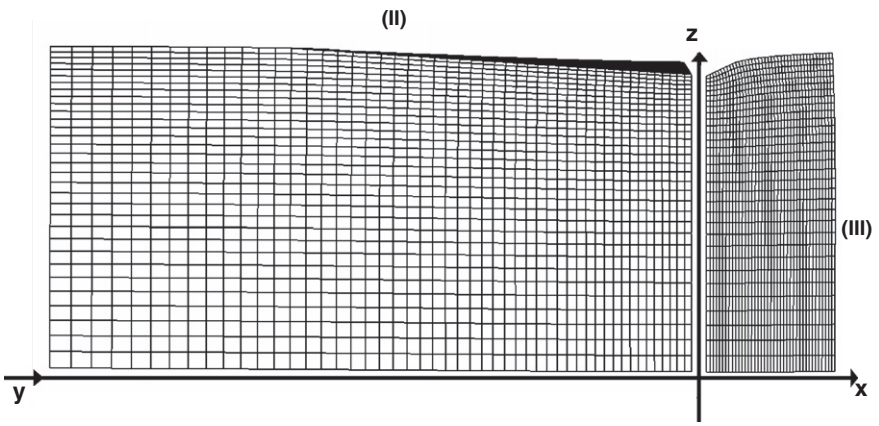


**Fig. 8.** Details of the deformed mesh for $\nu = 0.3$ at maximum load.

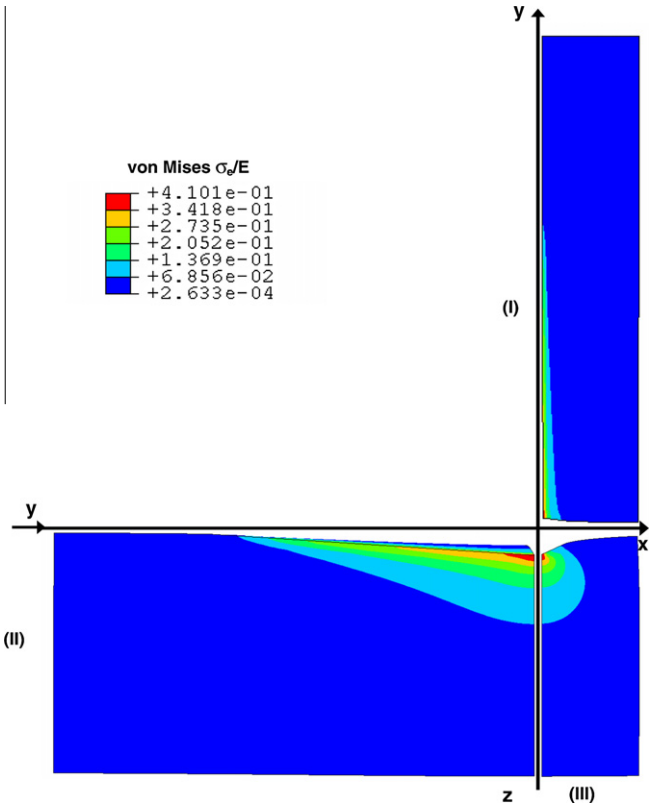


**Fig. 9.** Contours of dimensionless von Mises stresses $\sigma_e/E$ at maximum load for $v = 0.3$. The frictionless case ($\mu = 0$) is shown.

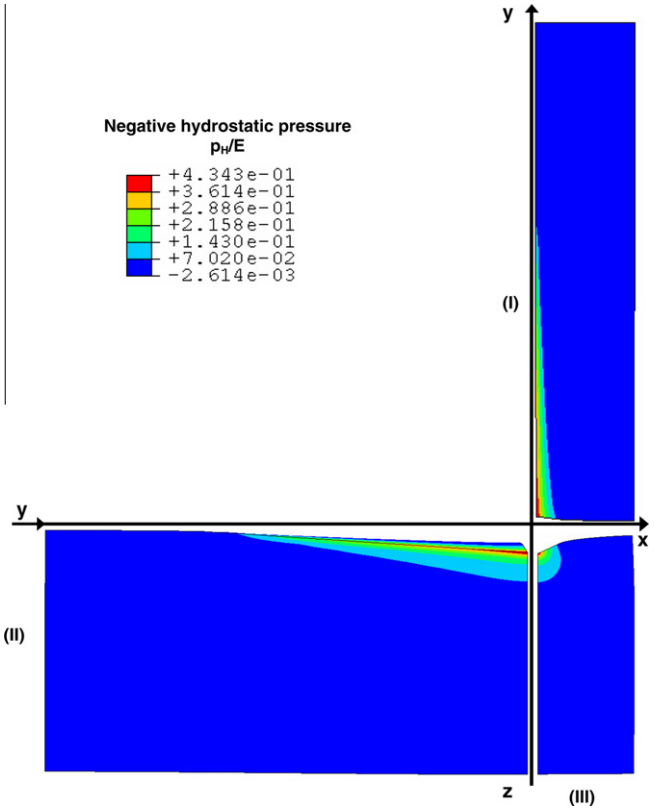


**Fig. 10.** Contours of dimensionless negative hydrostatic pressure $p_H/E$ at maximum load for $v = 0.3$. The frictionless case ($\mu = 0$) is shown.

the rate of numerical convergence of the solution and $A/h^2$ is almost unaffected by the level of Poisson ratio. These results may be viewed in accordance with Fig. 6 where isobars of the dimensionless contact stresses $\sigma_{zz}/E$ are shown for $v = 0.3$ and $h/h_e = 10$. These are essentially second Piola–Kirchhoff tractions and scale up with the average contact pressure $p_{av} = P/A$. The zero isobar of the normal stresses ($\sigma_{zz}/E = 0$) gives an accurate presentation of the contact area perimeter. Notice that for the Knoop indentation, $m/l$ (as defined in Fig. 1) is equal to 12.8. This result is in excellent agreement with experimental observations and analytical predictions presented by Giannakopoulos (2006) that give $m/l$ ratio of 12.5–13.18, respectively.

Next we explore the average contact pressure $p_{av}$ defined as the ratio of the applied load $P$ divided by the true projected contact area $A$ (i.e. computed contact area as viewed from the surface). It was numerically found that the average contact pressure is constant and is related to the elastic properties as:

$$p_{av}(1-\nu^2)/E = 0.1898(1 - 0.06625\nu + 0.03187\nu^2 - 0.2889\nu^3). \tag{8a}$$

For comparison we write the corresponding solutions for Vickers and Berkovich indentations (see Giannakopoulos et al., 1994; Larsson et al., 1996, respectively):

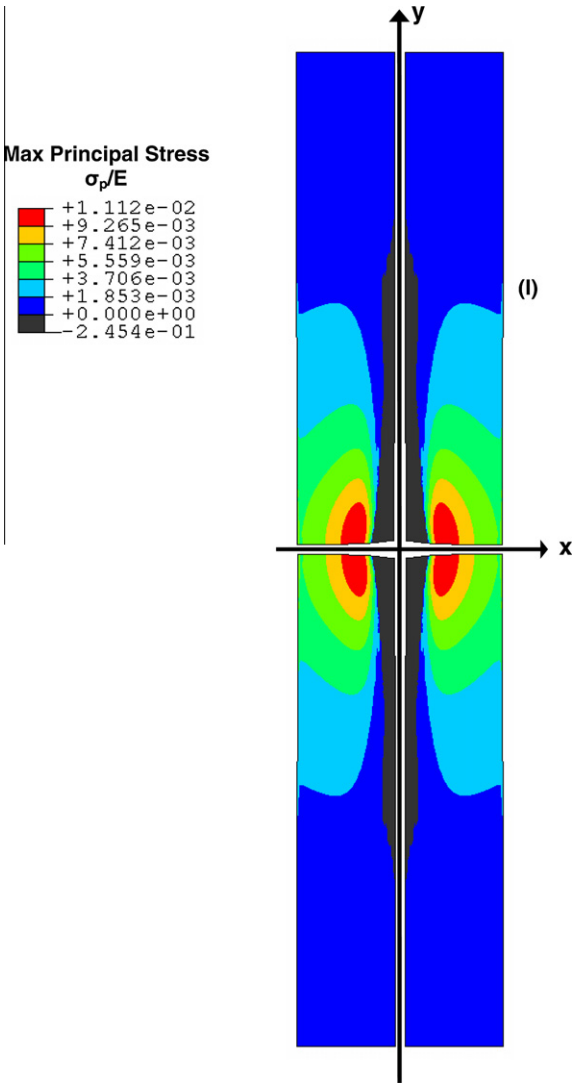


**Fig. 11.** Contours of dimensionless maximum principal stresses $\sigma_p/E$ at maximum load for $v = 0.3$. The frictionless case ($\mu = 0$) is shown.

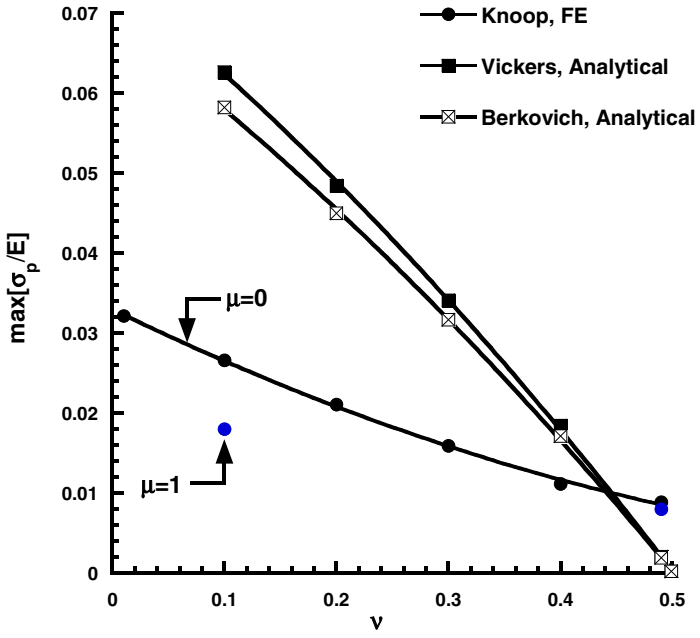


**Fig. 12.** Maximum principal stresses $\sigma_p/E$ as a function of Poisson ratio $\nu$ at $h/h_e = 10$ (maximum load). Corresponding results are given for Vickers and Berkovich pyramid indenters for comparison. The Knoop indenter works well in cases where surface cracking is to be avoided. The frictionless case ($\mu = 0$) is shown.

**Table 1**
Summary of the results for the pyramid indention for linear elastic incompressible solid.

| Parameter | $\phi_2$ | $\Theta$ | $m/l$ | $A/h^2$ | $\frac{C(1-\nu^2)}{E}$ | $\frac{P_{av}(1-\nu^2)}{E}$ | $\max\frac{\sigma_1}{E}$ |
|---|---|---|---|---|---|---|---|
| Vickers (analytical) | 45° | 68° | **1** | 9.86 | 1.79 | 0.182 | 0.0775 |
| Berkovich (analytical) | 60° | 65.3° | – | 9.64 | 1.84 | 0.191 | 0.0720 |
| Knoop (analytical) | 82° | 64.8° | 13.18 | 23.95 | 3.68 | 0.154 | 0 |
| Knoop (FE) | 85.79° | 65 | 12.8 | 23.92 | 4.42 | 0.184 | 0.0149 |

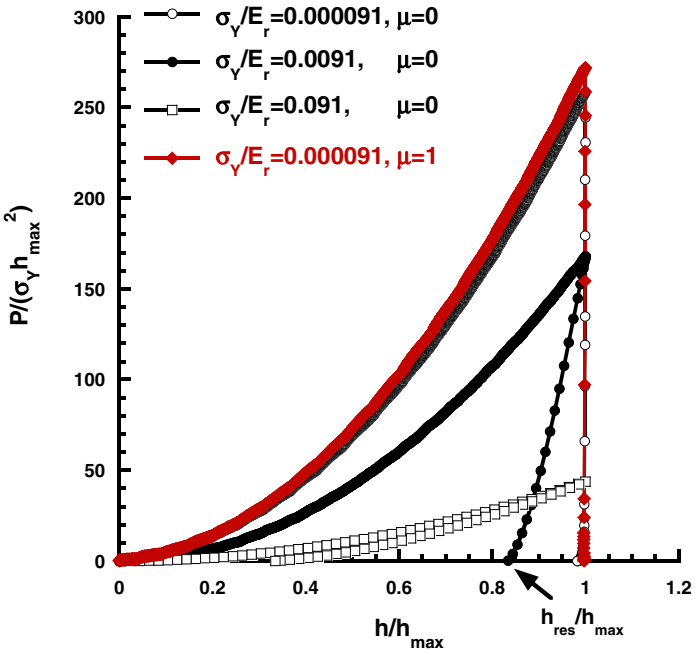


**Fig. 13.** Dimensionless load $P/\left(\sigma_Y h_{\max}^2\right)$ versus dimensionless indentation depth $h/h_{\max}$ for different values of $\sigma_Y/E_r$ ratio ($h_{\max}$ is the maximum indentation depth). We present results for Coulomb friction coefficient $\mu = 0$ and 1. In all cases $\nu = 0.3$.

$$p_{av}(1-\nu^2)/E = 0.2108(1-0.1655\nu-0.1737\nu^2-0.1862\nu^3), \quad (8b)$$

$$p_{av}(1-\nu^2)/E = 0.2201(1-0.21\nu-0.01\nu^2-0.41\nu^3). \quad (8c)$$

The results are shown in Fig. 7. The average pressure attained for the Knoop indenter is qualitatively similar to the corresponding solutions for Vickers and Berkovich indentations. The influence of $\nu$ is lower for the Knoop indenter (see related discussion on the influence of $\nu$ on $C$, Eq. (7)). Again the effect of Coulomb friction (data points for $\mu = 1$) is of minor importance.

As expected the deformation was found to scale directly with the indentation depth $h$ and the deformed mesh is shown in Fig. 8 for $\nu = 0.3$. Note the substantial sinking-in of the material, especially along the short contact radius in the $x$-direction. In-plane slipping was found at the contact area, which was not in a monotonic outward direction. At the contact region, the tangential displacements were very small compared to the vertical ones, except very close to the tip of the indenter, partly justifying the frictionless assumption.

Contours of characteristic stress fields give further insight of the problem. For $\nu = 0.3$ and $h/h_e = 10$, Fig. 9 presents the isobars of the normalized von Mises effective stress, $\sigma_e = \left(3/2\sigma'_{ij}\sigma'_{ij}\right)^{1/2}$, where $\sigma'_{ij}$ is the deviatoric Cauchy stress $\sigma'_{ij} = \sigma_{ij} - 1/3\sigma_{kk}\delta_{ij}$. Results are shown on the deformed configuration. Close to the contact region, the shape of the von Mises stress field is conical with an almost circular base on the $x$–$z$ plane and the apex on the long contact radius in the $y$-direction. The isobars of the normalized negative hydrostatic pressure $p = -\frac{1}{3}\sigma_{kk}$ are plotted again for $\nu = 0.3$ and $h/h_e = 10$, in the deformed configuration and presented in Fig. 10. Note that the hydrostatic and the von Mises stress fields are highly asymmetrical with respect to the loading direction, but tend, as expected to the Boussinesq point force solution away from the contact area. Finally, in Fig. 11 we present isobars of the normalized maximum principal stresses $\sigma_p/E$. The maximum principal stresses are tensile and appear at the contact perimeter exactly at the intersection of the hyperbolic contact boundary with the $x$-axis. The effect of the Poisson ratio upon the maximum principal stresses is shown in Fig. 12. Results are shown for the Knoop indentation and are compared with corresponding results for the Vickers and for the Berkovich according to Giannakopoulos (2006). Note that for increasing Poisson ratio the values of principle stresses drop as expected and they are always lower than the corresponding to the Vickers and Berkovich indenters. Note that $\sigma_p/E_r \to 0$ as $\nu \to 1/2$ where $E_r = E/(1-\nu^2)$, in accord with general aspects of linear contact mechanics Hills et al. (1993). As the symmetry of the pyramid indenter is increasing, the tensile stresses increase and reach the limit of the cone. This is in broad agreement with results presented in Giannakopoulos (2006). The Knoop indenter seems to work well in cases were surface cracking is to be avoided but under extremely brittle conditions cracking may be observed. It was numerically found that the maximum principal stress is constant and related to the elastic properties as:

$$\max(\sigma_p/E) = 0.03244(1-1.84\nu+0.3699\nu^2-0.308\nu^3). \quad (9a)$$

At the same points (middle of the contact hyperbolic arcs) the maximum tensile stresses are

$$\max(\sigma_p/E) = \frac{1-2\nu}{1-\nu^2}Z \quad (9b)$$

with $Z = 0.0775$ for the Vickers and 0.072 for the Berkovich indenters (see Giannakopoulos et al., 1994; Larsson et al., 1996, respectively). Sharp indenters could result in pronounced coupling of the vertical with tangential displacements. Georgiades (1998) analysed the two-dimensional contact of an obtuse wedge indenter and showed that at the indenter's tip the logarithmic contact stress appears. If a high Coulomb friction coefficient is assumed, a slight

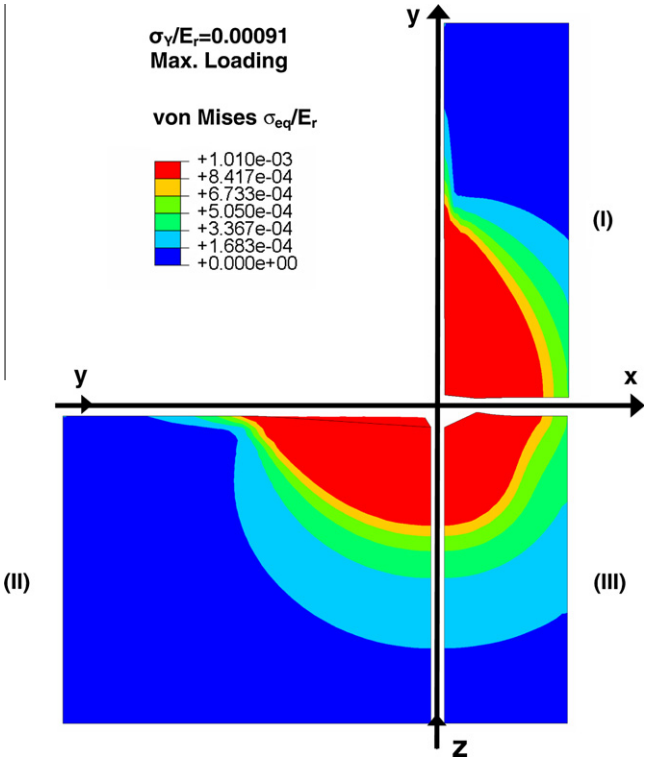


**Fig. 14.** Contours of dimensionless von Mises stresses $\sigma_e/E_r$ at maximum loading for $\sigma_Y/E_r = 0.00091$ ($\nu = 0.3$). The frictionless case ($\mu = 0$) is shown.

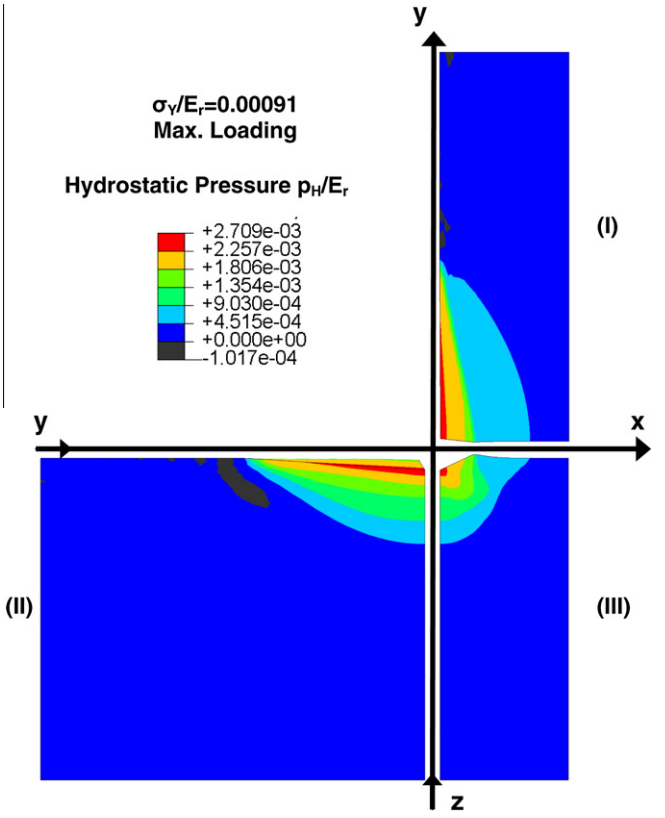


**Fig. 15.** Contours of dimensionless negative hydrostatic pressure $p_H/E_r$ at maximum loading for $\sigma_Y/E_r = 0.00091$ ($\nu = 0.3$). The frictionless case ($\mu = 0$) is shown.

drop at the stresses is observed. We investigated the issue of the finite stress value at the Knoop tip with FEM (absence of friction). The FEM solution does not allow the lateral surface displacements to penetrate the rigid sides of the indenter. At the tip, the contact stress $\sigma_{zz}$ $(x=0, y=0, z=0) \rightarrow -\infty$. This comes in contrast with the Vickers pyramid result of Giannakopoulos (2006), where $\sigma_{zz}$ was found to reach a finite value for $\nu \neq 1/2$.

The results of the present numerical work are summarized combined with analytical results for the Knoop and analytical and numerical results for the Vickers and Berkovich indenters, in Table 1. The results indicate that the normalised value of $C$ for the Knoop case is about twice the normalized value of $C$ as predicted by the Vickers, the Berkovich and the equivalent to the Vickers cone. The reason is that the Knoop pyramid has an elongated diagonal that forces the contact along this diagonal to resemble a 2-D wedge type of indentation and therefore to require a higher load in order to produce the same indentation depth. We must also note that the usual approach of an equivalent cone angle that fits the results for $C$ between the Knoop and the corresponding cone does not work in this case, because such an angle cannot retain the same average pressure $p_{av}$.

## 4. Elastoplastic analysis

In reality it is very difficult to make a purely elastic indentation and the materials will generally deform irreversibly and/or crack. In the current set of simulations the substrate deforms in an elastic-perfectly plastic manner and the response upon loading and unloading conditions is explored. Coulomb friction effects between the surface of the substrate and the indenter are also explored. Strain hardening effects are ignored and initial stresses (e.g. residual stresses) are not accounted in the present calculations. These will be dealt within a separate work.

The problem now has to be analysed within large strain formulation. Accordingly, the Prandtl–Reuss constitutive equations, to be integrated, are

$$\widehat{\tau}_{ij} = \frac{E}{1+\nu}\left(\delta_{ik}\delta_{jl} + \frac{\nu}{1-2\nu}\delta_{ij}\delta_{kl} - \frac{3\tau'_{ij}\tau'_{kl}\frac{E}{1+\nu}}{2\tau_e^2\left(\frac{2}{3}H + \frac{E}{1+\nu}\right)}\right)D_{kl}. \tag{10}$$

In Eq. (10), $H$ is the instantaneous slope of the uniaxial tensile Kirchhoff stress $\tau$versus the logarithmic plastic strain $\varepsilon_{pl}$. The

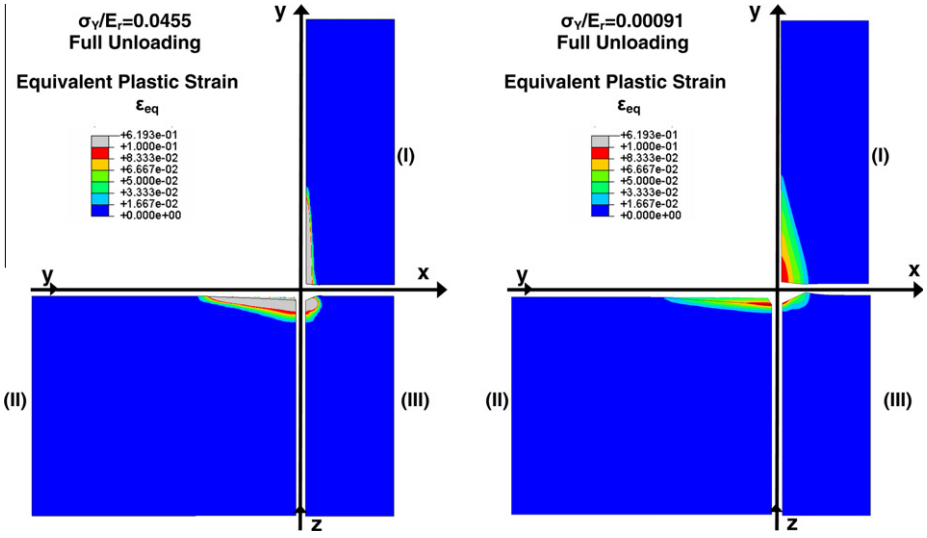


**Fig. 16.** Contours of equivalent plastic strain $\varepsilon_{eq}$ at complete unloading for $\sigma_Y/E_r = 0.00091$ and $\sigma_Y/E_r = 0.0455$ ($\nu = 0.3$).The frictionless case ($\mu = 0$) is shown.

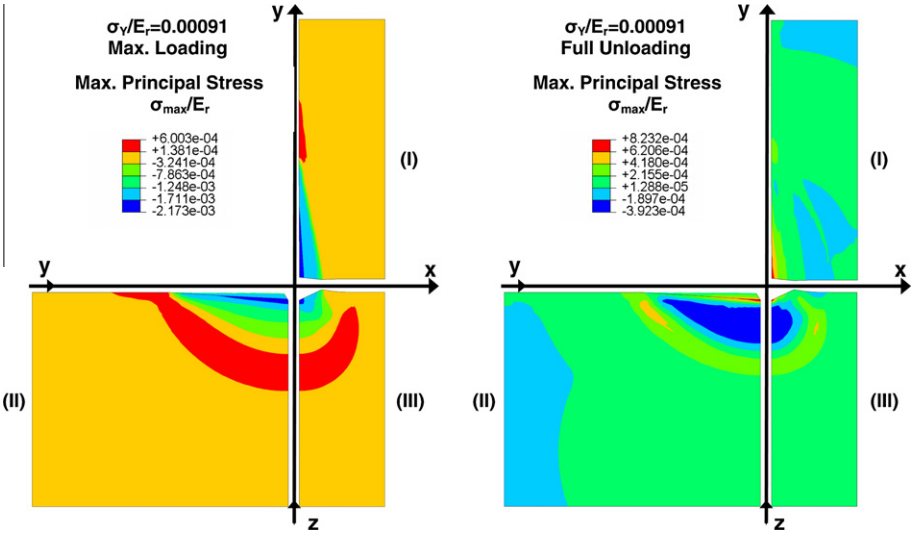


**Fig. 17.** Contours of dimensionless maximum principal stresses $\sigma_{max}/E_r$ at maximum loading and at complete unloading for $\sigma_Y/E_r = 0.00091$ ($\nu = 0.3$). The frictionless case ($\mu = 0$) is shown.

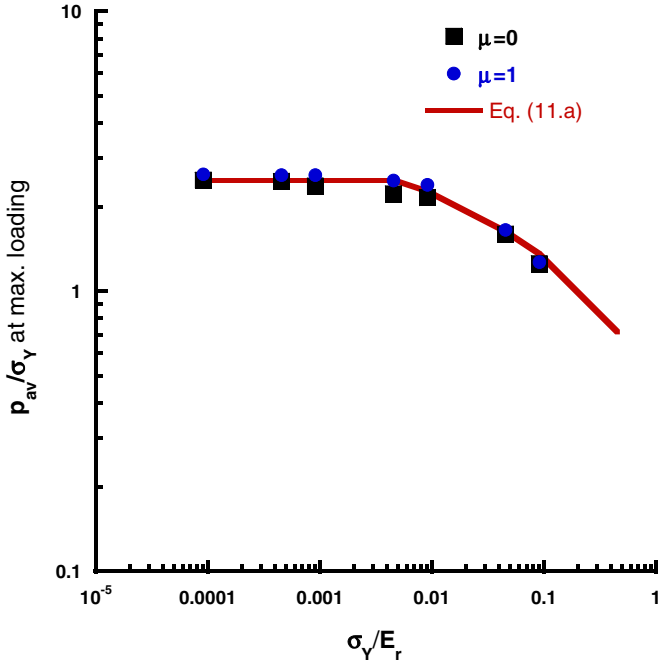


**Fig. 18.** Dimensionless average pressure $p_{av}/\sigma_Y$ at maximum loading as a function of the dimensionless ratio $\sigma_Y/E_r$. The corresponding solution for the Vickers indenter to Eq. (10) is added for comparison. Results are shown for Coulomb friction coefficient $\mu = 0$ and 1.

effective stress is $\tau_e = \left(\frac{3}{2}\tau'_{ij}\tau'_{ij}\right)$, where $\tau'_{ij}$ is the deviatoric part of the Kirchhoff stress. Additive decomposition of the total deformation rate in an elastic and a plastic part is assumed $D_{ij} = D^e_{ij} + D^{pl}_{ij}$. The accumulation of the plastic strain $\varepsilon_{pl}$ is measured from the line integral of the plastic part of the deformation rate $D^{pl}_{ij}$. Eq. (10) applies for the plastic loading where the effective stress is related to the axial response $\tau_e = \tau(\varepsilon_{pl})$. The yield stress condition is $\tau_y = \tau(\varepsilon_{pl} = 0)$. For the elastic loading or unloading Eq. (2) holds. The elastoplastic relations (10) apply reasonably well for low strain hardening (small values of $H/E$) in which case the elastic strains are much smaller than the plastic ones (Needleman, 1972). In the current study we will focus on elastic-perfectly plastic material behaviour ($H/E = 0$), implicitly assuming that $\left|D^e_{ij}\right| \ll \left|D^{pl}_{ij}\right|$ The constitutive law is homogeneous (elastoplastic properties independent of $X_i$).

The two most important features given by an indentation test is the load-indentation depth $P - h$ relation and the hardness (that is the average contact pressure $p_{av}$). Until now, universal formulae for these quantities at Knoop indentation have not been presented in the literature. We begin our analysis by presenting a set of load versus displacement curves. The results are presented in dimensionless form. In all cases presented we assume $\nu = 0.3$. Fig. 13 shows the dimensionless load $P\Big/\left(\sigma_Y h^2_{\max}\right)$ versus dimensionless indentation depth $h/h_{\max}$ for different values of the parameter $\sigma_Y/E_r$. We define $h_{\max}$ as the maximum indentation depth, $h_{res}$ as the residual depth and we remind the reader that $E_r$ as $E/(1-\nu^2)$. Increasing values of $\sigma_Y/E_r$ (that is decreasing Young's modulus or increasing yield strength) correspond to lower values of the dimensionless load $P\Big/\left(\sigma_Y h^2_{\max}\right)$ while the total amount of the elastic recovery increases. Furthermore, the friction between the surface of the half space and the indenter seems to be of minor importance, a conclusion that is consistent with previous indentation results, see for example Bower et al. (1993) and Li et al. (1993). (Again, we also used a Coulomb friction coefficient $\mu = 1$ in order to enhance any possible effect of friction.)

Further insight is given by exploring contours of characteristic variables of the problem. In order to present the contours, we unfold the three characteristic planes of the problem (I), (II) and (III) as explained previously. It is immediately observed that the projected contact area is quantitatively and qualitatively different from that attained for the pure elastic case. In Figs. 14 and 15 we present contours of the normalised von Mises stresses $\sigma_e/E_r$ and the negative hydrostatic pressure $p_H/E_r$, respectively, at maximum load and frictionless contact, for the case of $\sigma_Y/E_r = 0.00091$ ($\nu = 0.3$). It is observed that the elasto-plastic boundary is of

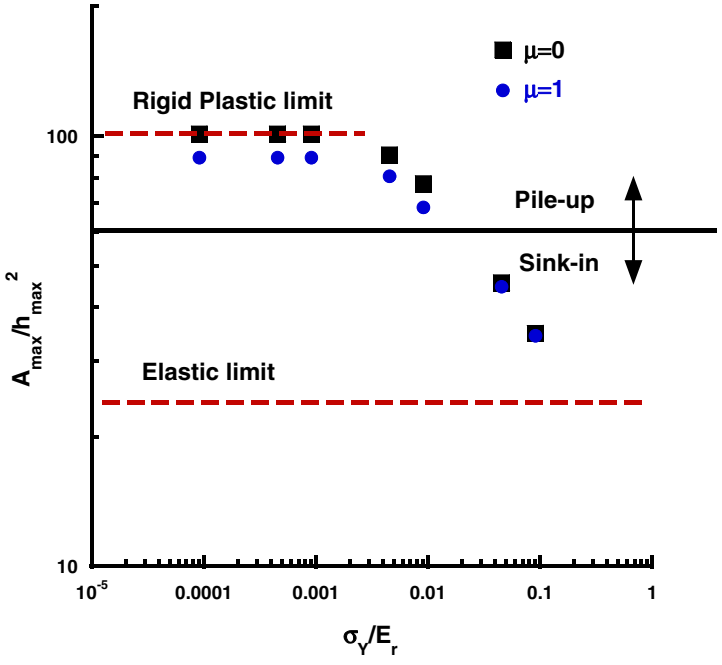


**Fig. 19.** Dimensionless contact area $A/h^2$ at maximum loading as a function of the dimensionless ratio $\sigma_Y/E_r$ ($\nu = 0.3$). Results are shown for Coulomb friction coefficient $\mu = 0$ and 1.

spherical shape for the von Mises stresses and of ellipsoidal shape for the hydrostatic pressure. The contours of equivalent plastic strain $\varepsilon_{eq}$ at full unloading for $\sigma_Y/E_r = 0.00091$ and 0.0455 are presented in Fig. 16. The plastic region and the elasto-plastic boundaries vary with $\sigma_Y/E_r$. For increasing $\sigma_Y/E_r$, the residual plastic region reduces on plane I, but increases on planes II and III. Furthermore, for decreasing $\sigma_Y/E_r$, the pile-up effect increases while for large values of $\sigma_Y/E_r$ a sink-in behaviour is attained. Finally, in Fig. 17 we present contours of dimensionless maximum principal stresses $\sigma_{max}/E_r$ at maximum loading and complete unloading for the case of $\sigma_Y/E_r = 0.00091$. Tensile stresses are attained below the plastic region due to the elastic unloading – see planes I and II. Nevertheless, the level of the attained tension is insignificant, thus the Knoop indentation method is beneficial when cracking is to be avoided in very brittle materials like ceramics. The above observations do not alter with increasing friction coefficient between the indenter and the surface thus we only present contours for the case that corresponds to $\mu = 0$.

One, very important information of the Knoop indentation test is the average pressure $p_{av}$, i.e. the hardness of the indented material. The average pressure is mainly affected by the ratio $\sigma_Y/E_r$. The effect of $\sigma_Y/E_r$ upon the hardness $p_{av}/\sigma_Y$ is shown in Fig. 18. Results are shown for frictionless contact and contact with friction coefficient $\mu = 1$. It is concluded that for $\sigma_Y/E_r \leqslant 0.03$, the

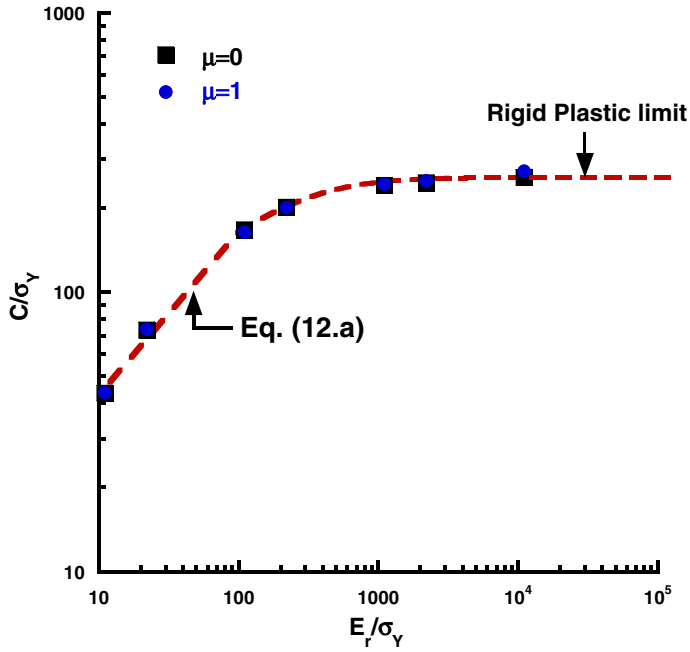


**Fig. 20.** Constraint factor $C/\sigma_Y = P/(\sigma_Y h^2)$ as a function of the dimensionless ratio $\sigma_Y/E_r$ ($\nu = 0.3$). Results are shown for Coulomb friction coefficient $\mu = 0$ and 1.

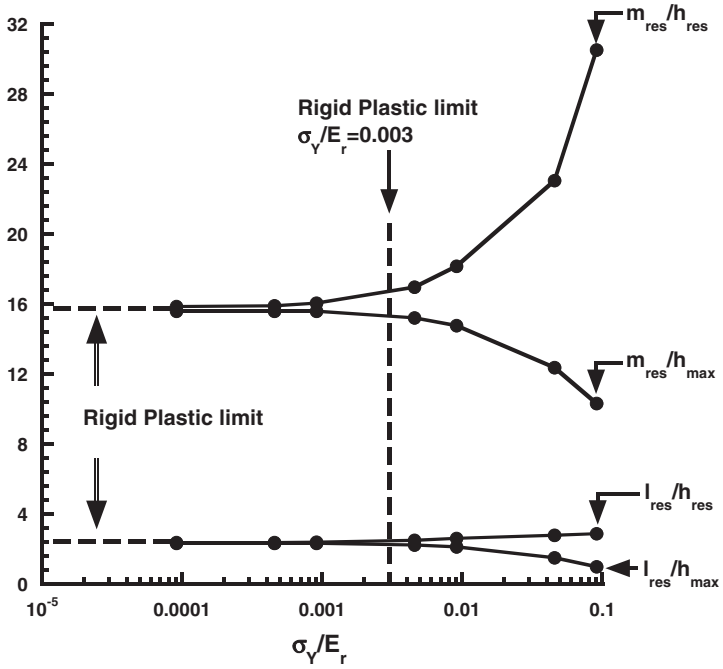


**Fig. 21.** Geometrical characteristics of the residual contact area – $m_{res}/h_{max}$, $m_{res}/h_{res}$, $l_{res}/h_{max}$ and $l_{res}/h_{res}$ as a function of the dimensionless ratio $\sigma_Y/E_r$.

dimensionless average pressure $p_{av}/\sigma_Y$ given from Knoop indentation is constant and equal to 2.5 (rigid plastic limit). For $\sigma_Y/E_r > 0.03$ the dimensionless average pressure drops with increasing $\sigma_Y/E_r$ and the whole dependence can be described according to the relation:

$$p_{av}/\sigma_Y = \min\left\{2.5, 0.4\left(1+\ln\left(\frac{E_r}{\sigma_Y}\right)\right)\right\}. \tag{11a}$$

For comparison, we present the analytical solution for the case of Vickers indentation; see Baxevani and Giannakopoulos (2009).

$$p_{av}/\sigma_Y = \min\left\{2.7482, 0.4667\left(1+\ln\left(\frac{E_r}{\sigma_Y}\right)\right)\right\}. \tag{11b}$$

The effect of the contact friction between the surface and the indenter is of minor importance.

The dimensionless contact area $A/h^2$, at maximum load, as a function of the dimensionless ratio $\sigma_Y/E_r$ is presented in Fig. 19. The elastic–plastic solution gives a larger contact area when compared to the one that corresponds to the purely elastic solution for small values of $\sigma_Y/E_r$, but for increasing $\sigma_Y/E_r$ the elastic solution is recovered. For, approximately, $\sigma_Y/E_r \leqslant 0.001$ the rigid plastic limit gives $A/h^2 = 101.9$. For increasing $\sigma_Y/E_r$ the dimensionless contact area approaches the elastic limit. Results are shown for Coulomb friction coefficients $\mu = 0$ and $\mu = 1$.

The dependence of the constraint factor $C/\sigma_Y = P/(\sigma_Y h^2)$ upon the ratio $\sigma_Y/E_r$ is presented in Fig. 20, for $\nu = 0.3$. In this case, for $\sigma_Y/E_r \leqslant 0.001$ the characteristic plateau of the rigid plastic limit gives $C/\sigma_Y = 258$. This result is about 2.5 times higher than the corresponding value for the Vickers indenter. Furthermore, the friction conditions between the surface of the indenter and the substrate surface are of minor importance. A good analytic fit for $\sigma_Y/E_r \geqslant 10$ is

$$\frac{C}{\sigma_Y} = 257\left\{1-\frac{1}{\pi}\Gamma\left[\frac{1}{0.29}, \left(\frac{E_r}{\sigma_Y}\right)^{0.29}\right]\right\}, \tag{12a}$$

where $\Gamma$ is the Gamma function.

For comparison, the analytical solution is added for the case of Vickers indentation (see Giannakopoulos et al., 1994).

$$\frac{C}{\sigma_Y} = 102.2\left\{1-\frac{1}{\pi}\Gamma\left[\frac{1}{0.29}, \left(\frac{E_r}{\sigma_Y}\right)^{0.29}\right]\right\}. \tag{12b}$$

Of particular importance for the Knoop experiments are the geometrical characteristics of the contact area, especially after the indenter has been removed. Thus in Fig. 21 we provide their dependence upon the dimensionless ratio $\sigma_Y/E_r$. The effect of the ratio $\sigma_Y/E_r$ upon $m_{res}/h_{res}$ and $l_{res}/h_{res}$ or $m_{res}/h_{\max}$ and $l_{res}/h_{\max}$ is explored, where $m_{res}$ and $l_{res}$ are the residual long and short diagonals and $h_{res}$ is the residual indentation depth. For $\sigma_Y/E_r \leqslant 0.003$, $l_{res}/h_{res} = l_{res}/h_{\max} = 2.3$ and $m_{res}/h_{res} = m_{res}/h_{\max} = 15.5$. For $\sigma_Y/E_r > 0.003$, $l_{res}/h_{\max}$ and $m_{res}/h_{\max}$ drop due to the elastic recovery of the substrate, but with a different rate so that $m_{res}/l_{res}$ increases (see Fig. 22). When the ratio $m_{res}/l_{res}$ is expressed as a function of the $p_{av}/E_r$ then the rigid plastic limit gives a constant value of $m_{res}/l_{res} = 6.7$ for $p_{av}/E_r \leqslant 0.003$. For increasing $p_{av}/E_r$, the ratio $m_{res}/l_{res}$ increases and approaches the elastic limit of $m_{res}/l_{res} = 12.8$ at $p_{av}/E_r = 0.184$.

Marshall et al. (1982) investigated the Knoop impressions on glasses, ceramics and metals, at ambient temperatures, and found that the long diagonal imprint ($m_{res}$) remains unchanged at elastic unloading (see also Fig. 23), whereas the short diagonal imprint contracts ($l_{res}$). The suggested experimental correlation between $m_{res}$ and $l_{res}$ is of the form

$$\frac{l_{res}}{m_{res}} \approx 0.1406 - 0.45\frac{p_{av}}{E_r}. \tag{13a}$$

Note that Marshall takes in place of $p_{av}$ the Knoop hardness $H_K = \frac{P_{\max}}{2ml}$ and $E$ in place of $E_r$, with $m$ and $l$ being the large and small diagonals respectively, giving,

$$\frac{l_{res}}{m_{res}} \approx 0.1406 - 0.45\frac{P_{\max}}{2mlE}. \tag{13b}$$

Eqs. (13a) and (13b) have been added in Fig. 22. We note that an excellent agreement is attained between the numerical and the experimental results for the case of Knoop indentation.

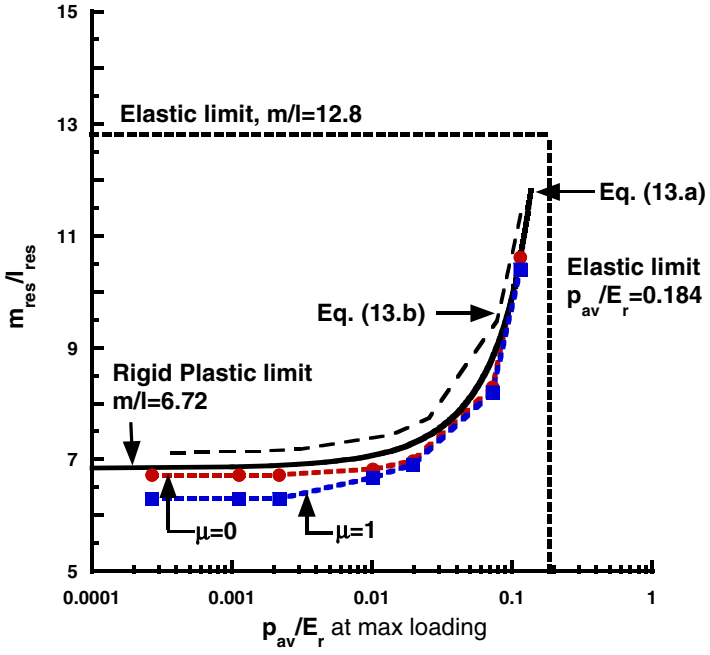


**Fig. 22.** Characteristic geometric ratio of the contact imprint after the complete removal of the indenter, $m_{res}/l_{res}$, as a function of the dimensionless average pressure $p_{av}/E_r$. The experimental relations according to Marshall et al. Eqs. (13a) and (13b) are added. Note that for Eq. (13b) the vertical axis corresponds to $P_{\max}/(2mlE)$ with $P_{\max}$ the maximum load and $m$ and $l$ the large and small diagonals respectively at maximum load. Results are shown for Coulomb friction coefficient $\mu = 0$ and 1.

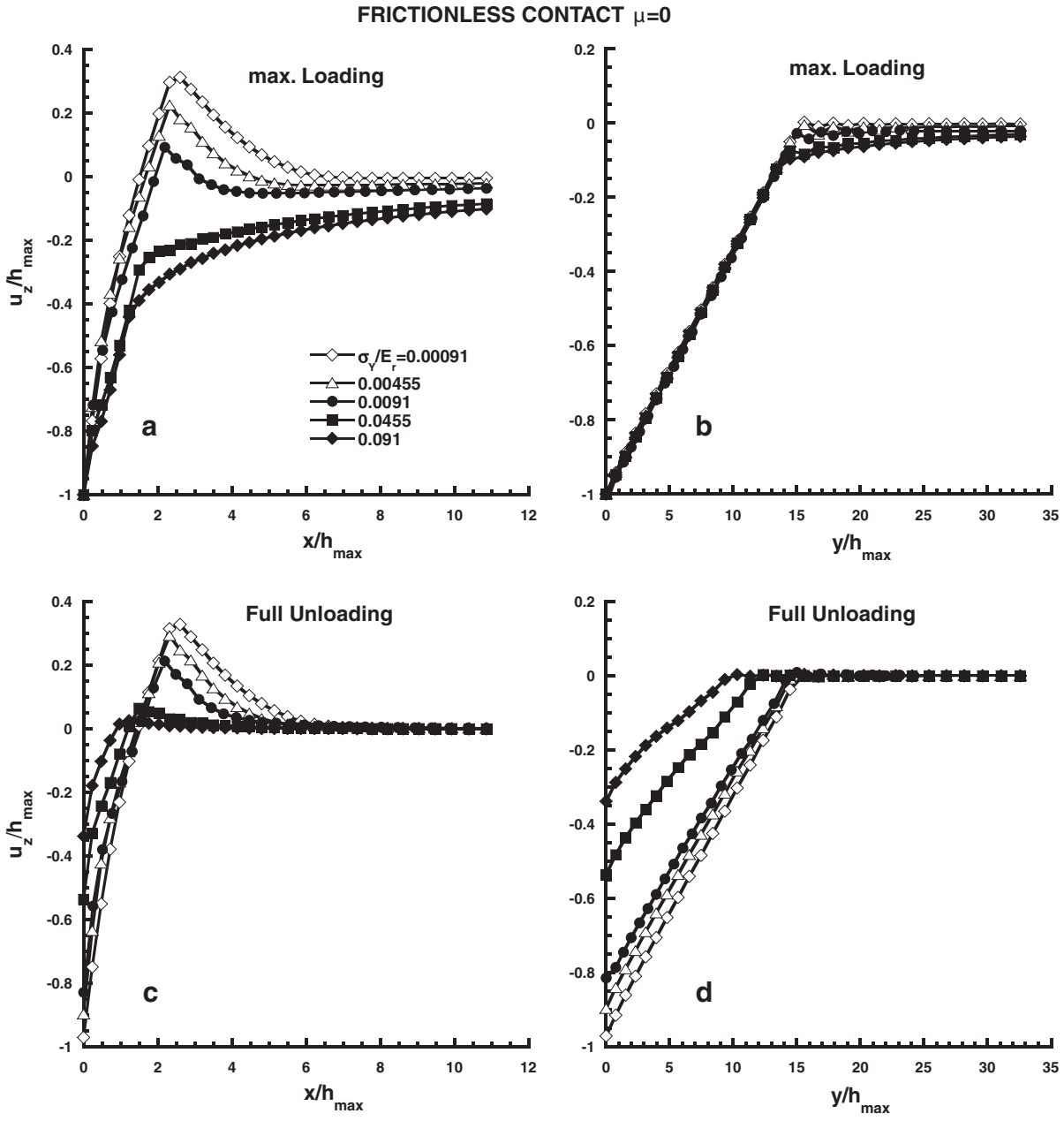


**Fig. 23.** Dimensionless deformation $u_z/h_{\max}$ along paths on the $x$- and $y$- axes (the shortest and longest contact radius respectively), for different values of $\sigma_Y/E_r$. Results are shown at the stage of full loading and at the stage of complete unloading. Results are shown the frictionless case ($\mu = 0$).

Furthermore, we note that the effect of friction between the indenter and the surface of the substrate is of minor importance (see results for $\mu = 1$), especially for $p_{av}/E_r \geqslant 0.01$.

Further insight on the pile-up or the sink-response of the surface and on the characteristics of the long ($y$-direction) and the short diagonal ($x$-direction) imprints is given in Fig. 23, for both maximum loading and full unloading. The dimensionless deformation $u_z/h_{\max}$ along the paths $(x,0,0)$ and $(0,y,0)$, for different values of $\sigma_Y/E_r$ are presented. What is of interest is the uneven response of the material at the two boundaries of the contact. Along the $(x,0,0)$ path, that is the short diagonal $2l$, sink-in succeeds the pile-up response with increasing $\sigma_Y/E_r$ (the critical value is $\sigma_Y/E_r \approx 0.032$). At the contact boundary along the $y$-axis i.e. the long diagonal imprint $(2m)$, the ratio $\sigma_Y/E_r$ slightly affects the response and the boundary remains pinned without significant pile-up or sink in for $\sigma_Y/E_r < 0.03$.

Finally, Fig. 24 gives the dimensionless residual indentation depth $h_{res}/h_{\max}$ as a function of the dimensionless average pressure $p_{av}/E_r$. The numerical results predict that when $h_{res}/h_{\max} \to 1$, that is when the elastic recovery vanishes (rigid plastic limit), then $p_{av}/E_r \to 0$. On the other extreme, for a fully elastic body the ratio $h_{res}/h_{\max} \to 0$, and the elastic limit is recovered with $p_{av}/E_r \to 0.184$. The indentation modulus $E_r$ can be correlated with the maximum indentation depth $h_{\max}$ and the residual depth of the indentation at the complete unload situation $h_{res}$ according to Eq. (14.a) as

$$\frac{h_{res}}{h_{\max}} = 18.154\left(\frac{p_{av}}{E_r}\right)^2 - 7.6411\frac{p_{av}}{E_r} + 0.9986. \tag{14a}$$

For the Vickers indenter, we have (Baxevani and Giannakopoulos, 2009)

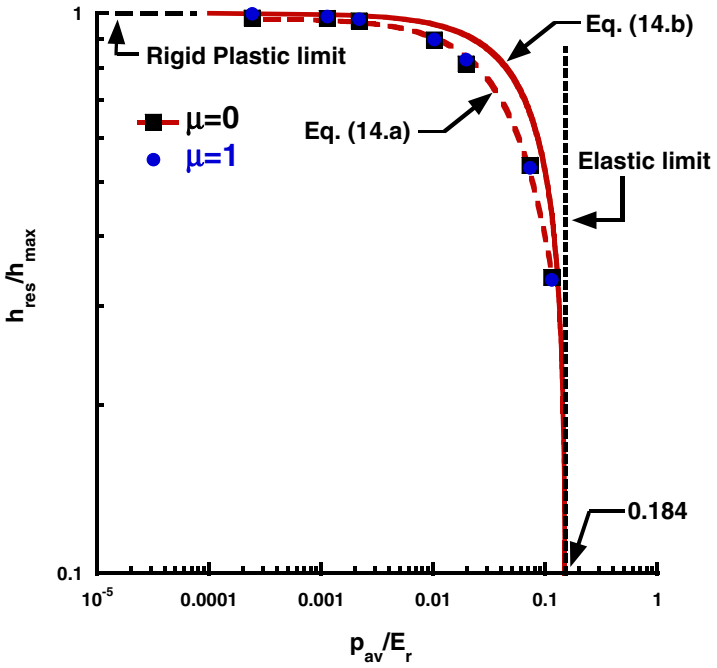


**Fig. 24.** Dimensionless residual indentation depth $h_{res}/h_{max}$ as a function of the dimensionless average pressure $p_{av}/E_r$. The experimental relation for the Vickers indenter according to Baxevani and Giannakopoulos is added, Eq. (14.b). Results are shown for Coulomb friction coefficient $\mu = 0$ and 1.

$$\frac{h_{res}}{h_{\max}} = -16.54\left(\frac{p_{av}}{E_r}\right)^2 - 3.0142\frac{p_{av}}{E_r} + 0.9785. \tag{14b}$$

Eq. (14.b) is close to Eq. (14.a) and has been suggested and experimentally verified by Breval and Mac Millan (1985), for many metals and ceramic materials, with no particular reference for power law type of strain hardening. Such approach gives a gross estimate of the modulus $E_r$, since it ignores the influence of the strain hardening exponent. An accurate estimate of $E_r$ would need to experimentally record the full unloading force-depth response, as obtained in instrumented indentation methodologies, see for example Oliver and Pharr (1992).

The ratio of the plastic to the total work $w_p/w_t$ relates to the ratio $h_{res}/h_{max}$ as

$$(h_{res}/h_{\max})^2 + 1.268(h_{res}/h_{\max}) - 2.2(w_p/w_t) = 0. \tag{15a}$$

This result is attained from numerical fitting of the results presented in Fig. 25. Note that for a fully elastic body $w_p/w_t = 0$, Eq. (15.a) predicts correctly $h_{res}/h_{max} = 0$, whereas for a rigid plastic body $w_p/w_t = 1$, predicts correctly $h_{res}/h_{max} = 1$.

The corresponding closed form estimate for Vickers indenter is given by Baxevani and Giannakopoulos (2009) as

$$(h_{res}/h_{\max})^2 + 1.5(h_{res}/h_{\max}) - 2.5(w_p/w_t) = 0. \tag{15b}$$

Note that the predictions of Eqs. (14.a) and (15.a) are insignificantly effected by friction.

Finally the slope $dP/dh$ of the load-indentation depth $(P-h)$ curve at the beginning of the unloading is frequently used by experimentalists as input to the circular punch elastic results of Sneddon (1945) when determining the elastic parameters of the indented materials, see for example Oliver and Pharr (1992). Fig. 26(a) presents the relation between, the dimensionless parameters $(1-\nu^2)/E1/\sqrt{A_{max}}dP/dh$ and $A/h^2$ at maximum loading. For $A_{max}/h^2_{max} \geqslant 80$, then $(1-\nu^2)/E1/\sqrt{A_{max}}dP/dh \approx 1.35$. Note that this is a different behaviour when compared to the corresponding results for the Berkovich and Vickers indenters where the same parameter is constant with $A_{max}/h^2_{max}$ and equal to 1.467 and 1.142, respectively (see Larsson et al., 1996 and Giannakopoulos et al., 1994). We believe that, because the Knoop indentation induces plasticity in a very anisotropic manner, the normalized $dP/dh$ relation is not constant with the ratio $A_{max}/h^2_{max}$. Another, perhaps more useful relation for experimental extraction of the elastic properties of the materials is presented in Fig. 26 (b). Here the parameter $(1-\nu^2)/E1/m_{res}dP/dh$ is connected with the geometrical characteristics of the residual contact area imprint $m_{res}/l_{res}$. Such a presentation suggests a direct connection between variables that can be directly measured at the end of each indentation exper-

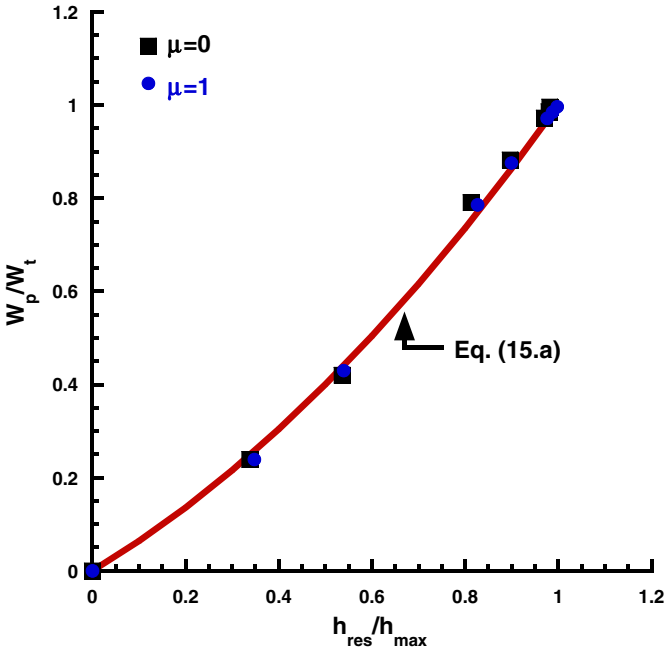


**Fig. 25.** The ratio of the plastic to the total work $w_p/w_t$ as a function of the ratio $h_{res}/h_{max}$. The corresponding solution according to Baxevani and Giannakopoulos is added according to Eq. (15.b).

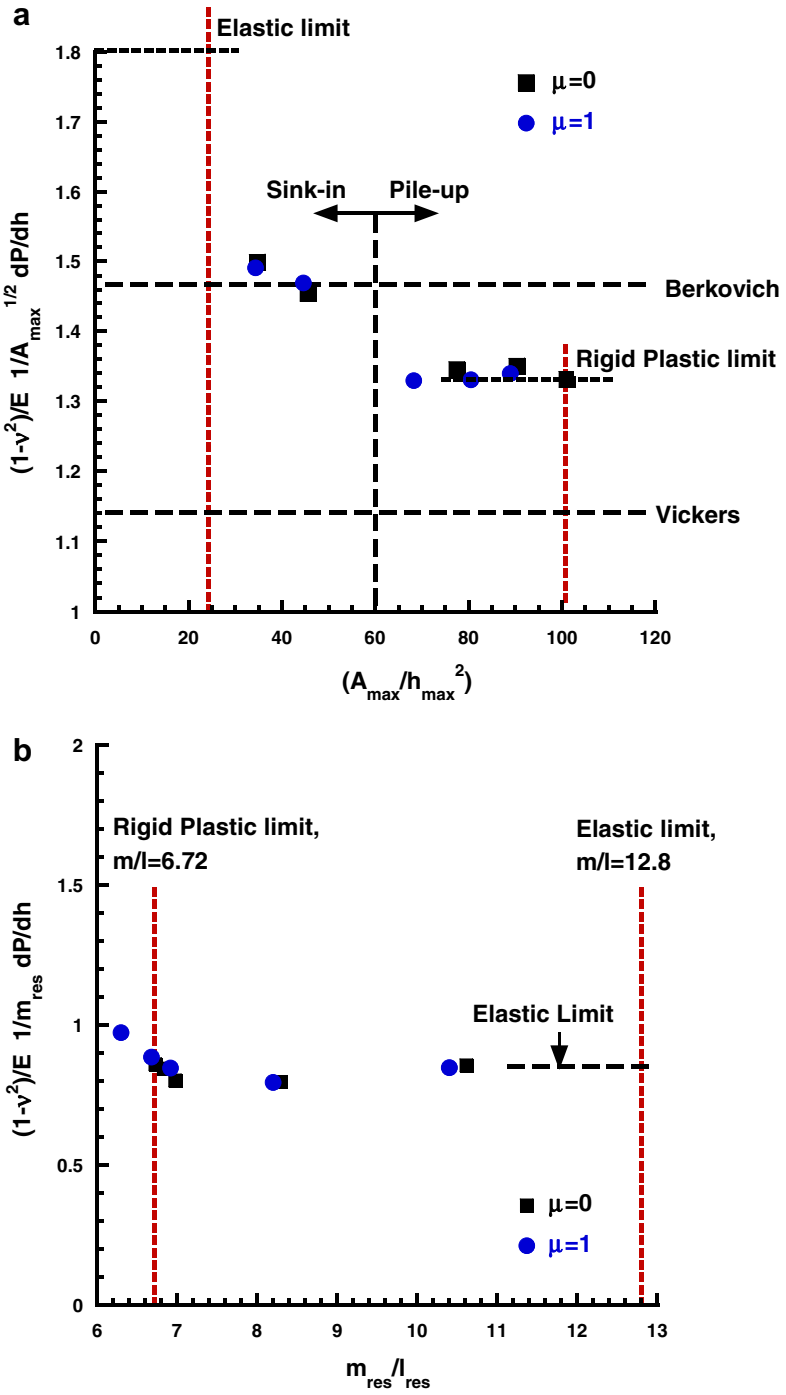


**Fig. 26.** (a) Relation between, the dimensionless parameter $(1-\nu^2)/E1/\sqrt{A_{max}}dP/dh$, and the dimensionless parameter $A/h^2$ at maximum loading. (b) Relation between, the dimensionless parameter $(1-\nu^2)/E1/m_{res}dP/dh$, and the ratio of the geometrical characteristics of the residual contact imprint $m_{res}/l_{res}$. Note that $dP/dh$ is measured at the initial stages of unloading.

iment – $m_{res}$, $l_{res}$ and $dP/dh$. Through Fig. 26(b) the material property $(1-\nu^2)/E$ can be readily extracted.

## 5. Conclusions

The scope of the present paper was to contribute to the analytic background on the use of Knoop indenters for mechanical characterization of materials. In the context of elasticity, only the hypoelastic response of the indented material is presented explicitly but small strain analysis was also carried out for reference purposes and gave similar results. Furthermore, the elastoplastic response was explored. Hooke's law was used for the elastic response and the Prandtl–Reuss equations for elastoplasticity without strain hardening. It is recognized that the undertaken mechanical analysis was phenomenological, in the sense that heat generation, dislocation activity in slip bands at individual grains, atomic reactions due to sharpness of the indenter and its associate compressive stress singularity, as well as other physical responses were not accounted for. In order for the present analysis to be realistic the indentation depths have to be much larger than any microstructure characteristic of the material or the indenter (e.g.

grain size and tip roundness). In the present analysis the steady state mechanical stresses and deformation fields were computed. Universal steady state relations between indentation load and depth were found for the elastic and the elasto-plastic response and the effect of Poisson ratio and the yield strength was evaluated respectively. Especially the $C = f(\sigma_Y/E_r)$ relation for the elastoplastic response is of great importance for experimental analysis. Furthermore, the average contact pressure for loading $p_{av}$ was found for the elastic response as a function of the Poisson ratio and for the elastoplastic response as a function of the ratio $\sigma_Y/E_r$. The projected contact area deviates from the geometric characteristics of the pyramid that are described by the normal rhomboidal base with ratio 1:7.11 to a ratio of 1:12.8 for the elastic regime of deformation. When elastoplastic behavior is assumed the short to long diagonal ratio of the residual imprint is equal to 1:6.72. With the present hardness testing instruments, the $P$–$h$ relation can be recorded and used for the assessment of material properties. Finally, possible cracking locations at loading were indentified in accordance with Knoop indentations of highly brittle materials, although the probability of Knoop induced cracking seems to be very remote, in accord with experimental results.

Furthermore, all our numerical results showed very good agreement with analytical and experimental results existing in the literature, in particular the well known Marshall et al. formulation that provides the modulus of elasticity directly from the ratio of the residual contact diagonals. General results as the ones derived in this work can serve many purposes, such as corrections of empirical hardness formulae and optimization of the indenters shape in order to minimize (or maximize) the damage induced into the indented material.

## References


ABAQUS version 6.2 (2001). User's Manual Hibbitt Karlsson and Sorensen Inc., Pawtucket RI.

Baxevani, E.A., Giannakopoulos, A.E., 2009. The modified Rockwell test: a new probe for mechanical properties of metals. Exp. Mech. 49, 371–382.

Berkovich, E.S., 1951. Three faced diamond pyramid for micro-hardness testing. Int. Diamond Rev. 11, 29–132.

Bower, A.F., Fleck, N.A., Needleman, A., Ogbonna, N., 1993. Indentation of a power law creeping solid. Proc. Royal Soc. 441, 97–124.

Breval, E., Mac Millan, N.H., 1985. Elastic recovery at Vickers hardness impressions. J. Mater. Sci. Lett. 4, 741–742.

Fischer-Cripps, A.C., 2002. Nanoindentation. Springer, New York.

Georgiades, H.G., 1998. Tangential displacement effects in the wedge indentation of an elastic half-space – an integral equation approach. Comput. Mech. 21, 347–352.

Giannakopoulos, A.E., 2006. Elastic and viscoelastic indentation by pyramid indenters. J. Mech. Phys. Solids 54, 1305–1332.

Giannakopoulos, A.E., Larsson, P.L., Vestegaard, R., 1994. Analysis of Vickers indentation. Int. J. Solids Struct. 31, 2670–2708.

Hills, D.A., Nowell, D., Sackfield, A., 1993. Mechanics of Elastic Contacts. Butterworth-Heinmann, Stoneham, MA.

Knoop, F., Peters, C.G., Emerson, W.B., 1939. A sensitive pyramidal-diamond toll for indentation measurements. J. Res. Nat. Bur. Stand. 23, 39–61.

Larsson, P.L., Giannakopoulos, A.E., Soderlund, E., Rowcliffe, D.J., Vestegaard, R., 1996. Analysis of Berkovich indentation. Int. J. Solids Struct. 33, 221–248.

Li, A., Ghosh, Y.H., Han, Bradt, R.C., 1993. The frictional component of the indentation size effect in microhardness testing. J. Mater. Res. 8, 1028–1032.

Marshall, D.B., Noma, T., Evans, A.G., 1982. A simple method for determining elastic modulus to hardness ratios using Knoop indentation. Int. J. Am. Ceram. Soc. A 65, C175–C176.

Mott, B.W., 1956. Micro-indentation Hardness Testing . Butterworth, London.

Murakami, Y., Tanaka, K., Itokazu, M., Shimamoto, A., 1994. Elastic analysis of triangular pyramid indentation by the finite element method and its applications to nano-indentation measurement of glasses. Philos. Mag. A 69, 1131–1153.

Needleman, A., 1972. A numerical study of necking in circular cylindrical bars. J. Mech. Phys. Solids 20, 111–127.

Olaf, J.M., 1993. Finite element analysis of indentation experiments. In: Proceedings of the First International Conference Contact Mech., pp. 69–76.

Oliver, W.C., Pharr, G.M., 1992. An improved technique for determining hardness and elastic modulus using load and displacement sensing indentation experiments. J. Mater. Res. 7, 1564–1583.

Rabinovich, V.L., Savin, V.K., 1996. Three dimensional modeling of indentation fracture in brittle materials. Mater. Sci. Eng. A 206, 208–214.

Smith, R.L., Sutherland, G.E., 1925. Some notes on the use of a diamond pyramid for hardness testing. Iron Steel Inst. 1, 285–304.

Sneddon, I.N., 1945. Boussinesq's problem for a flat-ended cylinder. Proc. Cambridge Philos. Soc. 42, 29–39.

Storakers, B., Larsson, P.L., 1993. On Brinnel and Boussinesq indentation of creeping solids. J. Mech. Phys. Solids 42, 307–332.

Tabor, D., 1951. Hardness of Metals. Clarendon Press, Oxford.

Wang, H., Bangert, H., 1993. Three dimensional finite element simulation of Vickers indentation on coated systems. Mater. Sci. Eng. A 163, 43–50.

Zeng, K., Rowcliffe, D., 1994. Identification of fracture sequences during sharp indentation of polycrystalline alumina. J. Mater. Res. 9, 1693–1700.